International Journal of Disaster Risk Reduction 106 (2024) 104403

Contents lists available at ScienceDirect

International Journal of Disaster Risk Reduction

journal homepage: www.elsevier.com/locate/ijdrr

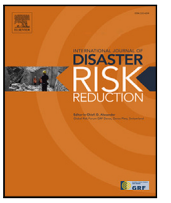

Quantitative assessment of earthquake-induced building damage at regional scale using LiDAR data

Fatemeh Foroughnia [a,*], Valentina Macchiarulo [a], Luis Berg [b], Matthew DeJong [b], Pietro Milillo [c,d], Kenneth W. Hudnut [e], Kenneth Gavin [a], Giorgia Giardina [a]

[a] Department of Geoscience and Engineering, Delft University of Technology, Stevinweg 1, Delft, 2628 CN, The Netherlands
[b] Department of Civil and Environmental Engineering, University of California, Berkeley, 760 Davis Hall, Berkeley, 94720-1710, CA, United States
[c] Department of Civil and Environmental Engineering, University of Houston, 4226 Martin Luther King Blvd, Houston, 77204, TX, United States
[d] Microwaves and Radar Institute, German Aerospace Center (DLR), Münchener Straße 20, Weßling, 82234, Germany
[e] Southern California Edison, Rosemead, 91770, CA, United States

ARTICLE INFO

Keywords:
Earthquake
Building damage
Damage assessment
Disaster management
Remote sensing (RS)
Airborne Light Detection and Ranging (LiDAR)

ABSTRACT

Regional-scale assessment of the damage caused by earthquakes to structures is crucial for post-disaster management. While remote sensing techniques can be of great help for a quick post-event structural assessment of large areas, currently available methods are limited to the detection of severely-damaged buildings. Furthermore, remote sensing-based assessment methods typically provide only qualitative results, as they lack integration with information on the building's behaviour in response to seismic-induced ground shaking. In this study, we developed a new methodology that uses airborne Light Detection And Ranging (LiDAR) data in combination with structural indicators of building response to provide a quantitative assessment of earthquake-induced damage at a regional scale. LiDAR datasets collected before and after an earthquake are used to measure residual displacements of building roofs. The resulting lateral drift estimations are used to quantify the level of damage for a specific building typology. Application to the LiDAR datasets collected before and after the 2014 earthquake in Napa Valley, California, demonstrates the capability of the proposed method to detect moderate levels of structural damage, proving its potential for faster and more accurate support to post-disaster management.

1. Introduction

Earthquakes are one of the deadliest natural hazards, with an average of more than 26 thousand deaths and $10 billion worth of damage per year in the last decade [1]. Most of these losses are caused by structural collapses [2]. The possibility to assess structural damage shortly after an earthquake is therefore essential to post-disaster management activities, both in the emergency response and recovery phases. For emergency response, an efficient assessment of structural damage can aid the rescue process and the identification of buildings that need to be access-restricted for safety purposes [3]. In the recovery phase, it enables the improvement of future seismic-resistant design by identifying the specific vulnerabilities of different building typologies [4].

As earthquakes generally impact extensive regions, building damage assessment needs to be conducted at a city or regional scale level. Typically, building-by-building visual inspections are performed by engineers during post-earthquake field reconnaissance

* Corresponding author.
E-mail address: f.foroughnia@tudelft.nl (F. Foroughnia).

https://doi.org/10.1016/j.ijdrr.2024.104403
Received 16 August 2023; Received in revised form 9 March 2024; Accepted 14 March 2024
Available online 22 March 2024

missions [5]. These missions are costly and time-consuming, especially if they need to cover large regions [6]. Thus, building damage assessment is often limited to sparse observations. A complementary solution to field inspections is the use of remote sensing (RS) techniques, which allow for the frequent acquisition of observations over vast regions, at a relatively low cost [7].

Different RS techniques can be employed to assess earthquake-induced building damage at a regional scale. Most assessment techniques are based on post-event data classification and multi-temporal change detection analysis to detect damaged buildings. Classification-based approaches involve datasets acquired after an event to identify and differentiate between damaged and undamaged buildings [8,9]. Change detection approaches are employed to analyse data collected before and after an earthquake, aiming to detect significant changes. These change detection methods are supplemented by a categorisation approach to classify the observed changes into different levels.

Classification approaches Primarily, RS-based studies have focused on detecting damaged urban areas using satellite imagery data, often employing optical spectral and Synthetic Aperture Radar (SAR) intensity data [10]. Post-event data classification approaches have predominantly used statistical features, like textures, to identify damaged structures. For example, in a study conducted by Gong et al. [11], first- and second-order statistical features extracted from Very High-Resolution (VHR) TerraSAR-X images were used to train machine learning classifiers for distinguishing between damaged and intact buildings. Ji et al. [12] used Conventional Neural Networks (CNNs) to detect collapsed buildings using a VHR QuickBird image taken after the 2010 Haiti earthquake. These CNNs were trained to recognise specific visual patterns and features associated with collapsed buildings. Bai et al. [13] employed machine learning algorithms for automatically mapping and classifying damaged buildings based on the statistical features from SAR ALOS-2/PALSAR-2 imagery. Despite the good performance of some classification approaches, their effectiveness heavily relies on the availability of ground-truth data to train the classifier for accurate classification across the entire area of interest [14].

Change detection approaches Various research efforts have focused on change detection approaches for earthquake impact assessment. Changes in building features such as shape, intensity, and texture obtained from pre- and post-event imagery data have been used for the detection of damaged buildings. In a recent study by Stephenson et al. [14], a deep learning-based forecasting technique was used to generate a distribution of co-event coherence, which represents the expected coherence in the absence of any damage. Coherence is a measure of the stability of the scatterers, e.g. buildings, and is defined by the spatial correlation between two SAR images. A reduction in the coherence image represents a loss of correlation between the pre-event and post-event data, indicating possible damage induced by the event. They conducted forecasts for individual pixels by analysing the time-series behaviour of pixels in the pre-event Sentinel-1 SAR data. This method enables the identification of anomalous drop in coherence by comparing the ground truth co-event coherence image and the forecasted one. In other studies, temporal information from sequential coherence SAR data before and during an earthquake was used to detect changes in structures. Karimzadeh et al. [15] analysed the differences between the coherence images using simple differencing and normalised differencing methods to assess the magnitude of the damage. Tamkuan and Nagai [16] combined differences in the coherence maps with the optical-derived spectral indices to identify damaged urban areas. In [17] the capability of damage mapping at the building level was examined by using an object-based change detection approach using QuickBird optical images before and after an earthquake. In their study, an existing urban map was used to identify image objects that correspond to the footprints of buildings. Their analysis incorporated a range of features that encompassed texture and colour changes, as well as statistical measures such as the Kullback Leibler Distance and Mutual Information, which capture similarity and correlation aspects. The results showed that textural features and changes in colour performed as the most effective in identifying damaged buildings.

LiDAR-based change detection Additionally, change detection approaches leveraging airborne Light Detection And Ranging (LiDAR) elevation data have been also used to classify collapsed buildings [18–20]. LiDAR sensors emit a laser pulse towards the ground surface and record the time for the reflected pulse to return to the sensor, resulting in the distance and 3D measurements of ground target locations. The vertical and horizontal Root Mean Square Errors (RMSEs) of the LiDAR observation points typically range from 5 to 10 cm and 10 to 25 cm, respectively [21]. In previous studies, damaged buildings were classified by detecting changes in the average height of buildings from LiDAR-derived Digital Surface Models (DSMs) before and after an earthquake. As earthquakes typically induce ground horizontal shifts, this technique requires the determination of corresponding points between pre- and post-event DSMs to quantify elevation changes. A preliminary horizontal alignment of the two DSMs might be therefore added to estimate this shift [18]. Note that by this approach it is only possible to detect damage that involves a notable variation in the building height [22].

While these approaches are effective in distinguishing between collapsed or severely damaged and undamaged buildings, they fall short in accurately measuring the extent of damage, particularly when it comes to slight or moderate damage levels. This limitation arises from the reliance on the building roofs' physical attributes, such as their height, slope, shapes, pattern, and texture. Consequently, these methods are only capable of identifying significantly damaged structures, which are discernible through changes in remote sensing imagery. For instance, severe damage or complete collapse can be indicated by the disappearance of a building footprint, a significant reduction in building height, or the presence of rubble and debris in the surrounding areas. Since they cannot provide insights into the failure mechanisms of structures, these approaches are inadequate for quantifying the extent of damage. Therefore, accurately measuring damage in quantitative terms and evaluating slight to moderate damage levels remains a challenge.

To quantitatively assess building damage across various levels, including slight to moderate damage, a more effective performance indicator is the measurement of displacements, which are directly connected to building deformations and can aid in identifying failure mechanisms. For instance, lateral drift measurements, derived from building displacements, are commonly used to measure the extent of damage caused by flexural and shear seismic-induced mechanisms [23]. The peak drift ratio, defined as

the ratio of the maximum roof drift to the building height, has been proven effective for a rapid evaluation of earthquake impacts on buildings [23–25]. As the peak drift can only be measured through a monitoring system in place on the building during the seismic event, its estimation is not practically applicable to most buildings [24]. A more practical indicator is the residual drift, which corresponds to the building's permanent displacement measured at the end of the seismic event [23,26].

Building displacements can be measured by differential LiDAR-based approaches. Since the 3D coordinates of the ground surface targets are measured by LiDAR sensors, pre-and post-event LiDAR data can be used to obtain 3D ground surface displacement measurements regardless of fault ruptures and displacement magnitudes, as demonstrated in [21,27–30]. Two differential approaches can be employed to generate displacement vectors by using LiDAR observations: the Particle Image Velocimetry (PIV) method and the Iterative Closest Point (ICP) method.

The PIV method, originally developed in fluid mechanics, determines the displacement vectors of fluid particles within a given space by finding correlations between images of the particles acquired over a short time span [31]. This method has been adopted in seismic applications to obtain seismic-induced displacement vectors using LiDAR data [32–35]. It requires the utilisation of pre- and post-event LiDAR datasets, such as intensity or elevation imagery data, to perform a spatial cross-correlation analysis between the two datasets, and estimate the occurred displacements. However, as LiDAR observations are recorded as discrete points, an additional step of creating 2D images through gridding or smoothing of the point observations is required. Consequently, not only the method fails to provide displacement measurements for buildings separately, but the smoothing process might lead to the introduction of biases within the displacement results [21].

The ICP method, on the other hand, uses the point observations to align two 3D point clouds by minimising the distance between the clouds [36,37]. The method has the potential to be adopted for monitoring ground seismic displacements using airborne LiDAR clouds [21,30], based on the assumption that the transition vector aligning the two clouds before and after an earthquake is equal to the earthquake-induced ground surface movement. Unlike the PIV method, the ICP method can theoretically provide also direct measurements of building displacements by aligning two point clouds acquired at different times. Since each cloud includes height information, it is possible to separate points on building roofs from points at the ground level to estimate the displacement vectors for each building individually. Various studies have used the ICP technique in earthquake-related applications [21,30], focusing specifically on the estimation of earthquake-induced deformations of the ground surface. However, these studies did not address the measurements of earthquake-induced structural deformations in buildings. To the authors' knowledge, the study conducted by Zieher et al. [38] is the only research which applied the ICP technique to LiDAR building observations, but to assess landslide-induced changes in a small area.

In this study, we exploited the potential of the ICP method to design a novel approach for quantitatively assessing building damage after an earthquake. As opposed to qualitative observation-based methods, we developed a methodology capable of detecting moderate levels of damage on a large scale by integrating RS LiDAR data with structural analysis. Our approach involved analysing LiDAR data acquired before and after the earthquake to determine the residual displacements of buildings. Building displacement measurements allow for identifying levels of damage that are not directly visible through RS images or height data. The method classifies different levels of damage by converting the building residual displacements to drift measurements, enabling a regional-scale damage classification that includes slight to moderate damage levels. We evaluated the performance of the proposed methodology by using LiDAR datasets acquired before and after the 2014 South Napa earthquake in California. Results were compared to observations from field investigations [27,39].

2. Case study and datasets

On August 24, 2014, a magnitude 6.0 earthquake struck the North San Francisco Bay Area, California. The epicentre was located to the south of Napa Valley at N38.220 W122.313, roughly 8 km south-southwest of the City of Napa, at a depth of approximately 11 km [40]. The earthquake ruptured the ground surface along several strands of the West Napa Fault zone, which is part of the larger San Andreas Fault Zone System. The surface rupture had a length of 12–15 km, extending northward from Cuttings Wharf town to Alston Park, in the City of Napa (Fig. 1). The 2014 South Napa earthquake was the first to cause substantial surface ruptures in Northern California since the 1906 San Andreas event. A co-seismic slip of 1.5 to 46 cm occurred along the earthquake rupture, which was predominately right lateral [41].

The City of Napa was among the most affected areas. At least $300 million worth of economic impact was observed on private and commercial properties, while public infrastructures incurred damage amounting to $58 million [45]. Damage was observed from the Browns Valley residential neighbourhood to the east of the downtown area, where some residential buildings exhibited shifts on foundations, wall cracks and chimney collapses. In Napa downtown, some historical masonry buildings were also severely damaged [46]. The area of interest for this study (Fig. 1) is located in the south part of the Browns Valley neighbourhood and includes wood-frame structures [47], which mostly suffered from cracked walls, and fallen or cracked chimneys [46].

LiDAR data We used two point clouds acquired before and after the earthquake. The pre-earthquake dataset was collected on June 7th, 2014, over Napa County by an airborne Leica ALS60 with a nominal point density of 8 $\mathrm{pts/m^2}$. The data was initially in the Coordinate Reference System (CRS) of NAD83 California State Plane Zone II with units of survey feet and NAVD88 orthometric elevations.

Following the 24th August earthquake, a post-earthquake dataset, distributed by OpenTopography [48], was acquired on the 9th of September by an Optech Orion M300 scanner, achieving point densities of approximately 11.4 $\mathrm{pts/m^2}$ [29]. The elevation observations obtained from the post-event LiDAR were validated by the vendor through the use of eight ground control points,

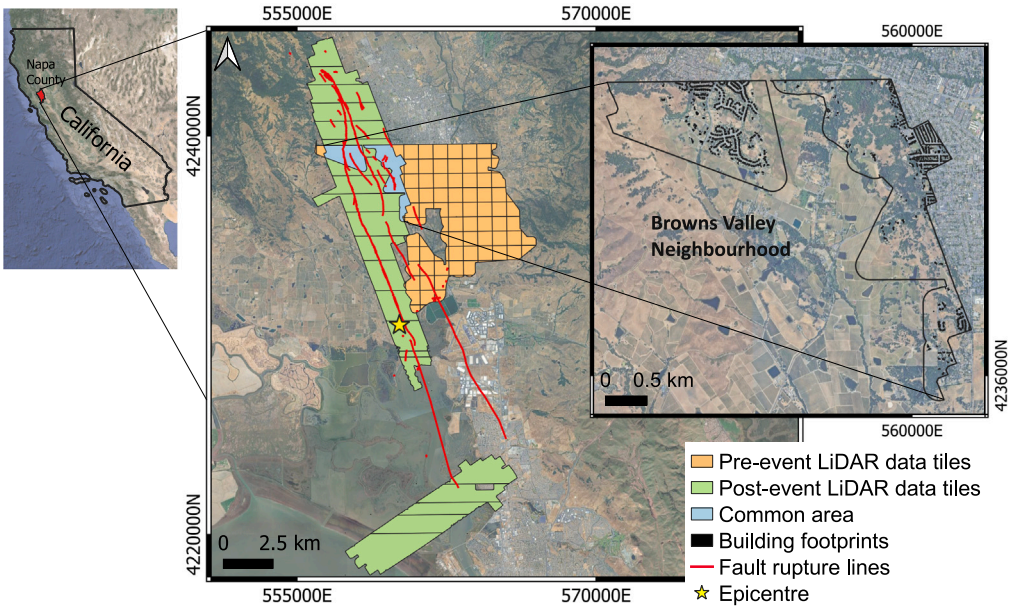

Fig. 1. Case study area, showing the regions covered by pre- and post-event LiDAR data. Red lines indicate fault ruptures [42]. The black polygons refer to building footprints, obtained from OpenStreetMap (OSM) [43] data layer and the Napa municipality [44]. (For interpretation of the references to colour in this figure legend, the reader is referred to the web version of this article.)

demonstrating high accuracy and an error of approximately 1.2 cm. The post-event data was projected in the CRS of NAD83 UTM Zone 10N, with both horizontal and vertical measurements in metres. Consequently, to ensure consistency, we also transformed the pre-event data to match the CRS of the post-event dataset. The classification of the post-event point cloud was carried out by the vendor using the TerraScan software. The software classifies ground points by creating a triangulated surface model. Points that were within 5 cm of the triangulated ground surface were incorporated into the model, resulting in a sparse ground model containing some artefacts. To remove the artefacts from the sparse ground model, points that were up to 15 cm from the ground model were added, leading to the creation of a denser and more accurate ground model [49].

The post-event data was originally classified into seven classes: unclassified, ground, low vegetation, medium vegetation, high vegetation, building, and outlier points, according to the Terrascan's proprietary algorithm based on specified setting parameters. However, the pre-event data had not been classified prior to this analysis. The classification of the data was conducted by using LASTools functions implemented in a Quantum Geographic Information System (QGIS) environment [50]. We first identified the ground points and then classified the building points based on their height information.

The geographical extent of the two surveys is shown in Fig. 1. This study focuses on the overlapping area covered by both surveys, equal to approximately 4.7 km^2 (Fig. 1).

Building footprint dataset Building footprint layers were used to extract the roof observation points from the LiDAR building clouds. The commonly used data source for this purpose is the OpenStreetMap (OSM) building footprint layer [43]. However, the OSM layer did not include all buildings within the area of interest. To address this limitation, we used the footprints provided by the Napa Municipality [44]. As the Municipality layer does not accurately represent the real shapes of building roofs, we combined the two footprint layers into one, using the Municipality data only for areas without OSM footprints, aiming to extract as many buildings as possible. In total, we extracted 684 buildings for the damage level assessment, as shown in Fig. 1.

Field data The U.S. Geological Survey (USGS) team carried out field measurements during the three months following the 2014 South Napa earthquake. Their findings, detailed in [27], included an evaluation of afterslip observations, an investigation of seismic shaking-related damage in the downtown area, mapping of fault strands, which are active or might be a threat to future ruptures, and geospatial information based on imagery data, such as aerial photographs, airborne LiDAR data, medium-resolution Landsat-8 and SPOT-6, and high-resolution WorldView-2 and QuickBird-1 optical images. To evaluate our work, we used the lateral ground offset displacements as the ground truth.

Furthermore, the California Governor's Office of Emergency Services (Cal OES) conducted field inspections to assess building damage. These inspections resulted in a dataset in which some buildings were restricted in use (yellow-tagged), and others were deemed unsafe (red-tagged). The building tagging data consists of 1572 yellow- and 152 red-tagged structures and is available at Cal OES [39]. Geospatial records of inspected buildings show that red and yellow tags were distributed across the City of Napa, from the west of the Browns Valley to the east of the Napa River [46]. Most red-tagged structures were located in downtown Napa, where pre-LiDAR data was not available. Fig. 2 shows the distribution of tagged buildings within our region of interest. Within this

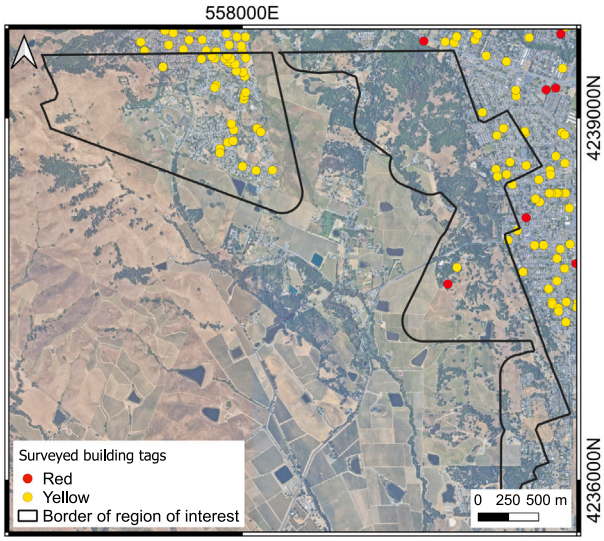

Fig. 2. Distribution of yellow- and red-tagged buildings in the region of interest. (For interpretation of the references to colour in this figure legend, the reader is referred to the web version of this article.)

area, 39 buildings were tagged, with 38 yellow-tagged and one red-tagged. No tagging information was available for the remaining buildings.

3. Methodology

We developed a new methodology for quantifying the extent of building damage at a regional scale by using RS LiDAR data. Our approach combines LiDAR-derived displacements with structural analysis to derive building drift measurements. These measurements enable to categorise the level of damage for each building. Fig. 3 depicts a visual schematic representation of the proposed methodology.

The proposed method first classifies the LiDAR clouds to extract the ground and building points. The ICP registration method [36] is then applied to pre- and post-event ground and building points to obtain 3D displacement vectors. We designed two strategies of point-based and window-based alignment in the ICP approach to process the building and ground point clouds, respectively. In the building cloud processing, an estimation of 3D displacements was obtained for each roof point individually. LiDAR observations of buildings consist of coordinates of the roofs, indicating building positions on the ground. Hence, the transition vectors obtained from the ICP alignment of the roof points also include the contribution of ground displacements. For this reason, we estimated the ground displacements to subtract them from the building displacements. The application of the ICP method to estimate ground displacements was inspired by the window-based ICP registration as described in [21]. As the ground deformations might vary with the distance from the fault, we divided the datasets into $100\,\mathrm{x}100\,\mathrm{m}^2$ windows and then applied the point-based ICP to all point observations within each window separately.

After separating the X and Y displacement components, the residual building displacements, i.e. displacements at the building level after removing the ground components, were derived. Finally, we determined the level of damage for each building by correlating these residual building displacements with residual drift ratios.

The ICP approach and the subsequent steps of damage quantification are described as follows.

Iterative Closest Point (ICP) In the ICP algorithm, one cloud is considered fixed as a reference cloud, and the other as a target cloud. The ICP aligns the target cloud with the reference one iteratively [36]. In this study, we assumed the post-event point cloud as the reference cloud, while the pre-event cloud was the target one.

First, we used the KD-tree nearest neighbour algorithm [51] to identify the closest corresponding point in the reference cloud for each point in the target cloud. Second, we applied a point-to-point rigid body transformation function to the target cloud, including a transition vector and a rotation matrix. The function minimises an error metric, i.e. Mean Square Error (MSE), between all corresponding pairs. The target cloud iteratively converges toward the reference set as the correspondences progressively improve. The procedure of determining correspondences and computing the transformation repeats until the MSE does not change any longer or reaches a predefined threshold. This corresponds to a linear least-square problem that was solved robustly by the Singular Value Decomposition (SVD) method [28]. The algorithm also reduces the impact of outliers by adding weight to corresponding pairs based on the distance criterion [52]. For each point, the displacement vectors are the summation of transition vectors in horizontal and vertical directions over the iterations.

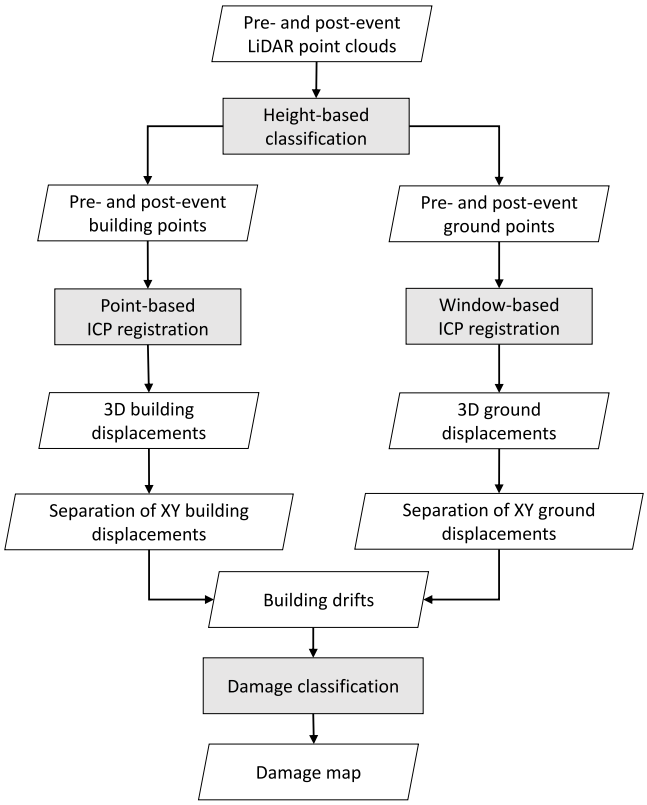

Fig. 3. Flowchart of the proposed approach.

As misclassified points and outliers, e.g. vegetation can negatively affect the registration result, we added a rejection step to exclude invalid correspondences from the ICP chain processing. The rejection step filters out the false correspondences based on distance and normal vector compatibility criteria.

Drifts and damage classification A buffer of 4 m was used to extract the points around each building. We then calculated the average ground displacements of the points within the buffers. To obtain the residual building displacements, the average ground value was subtracted from the displacements of each building point. To estimate the residual drift ratios D, we first calculated the average value of residual building displacements of all roof points in the X and Y directions separately. The maximum average value was then divided by the average building height to obtain the drift ratio for each building. The building height was estimated by subtracting the average Z coordinates of ground points within the buffer from the average Z coordinates of the roof points. Finally, the drift ratios were used to classify the level of damage to buildings from slight to complete.

As the building stock analysed in this work consists of wooden frame structures, we used the damage level classification included in [53] for the same structural typology. Specifically, the damage level was categorised as negligible for $D < 0.42\%$, slight for $0.42\% \leq D < 1\%$, moderate for $1\% \leq D < 3.2\%$, extensive for $3.2\% \leq D < 7.9\%$, and complete for $D \geq 7.9\%$. This classification is based on the Hazards US (HAZUS) loss estimation approach [54] to assess earthquake damage to buildings. The slight and moderate levels of damage refer to small and large cracks at the corners of openings, respectively. Extensive damage corresponds to large diagonal cracks and residual displacements in shear walls, while large permanent deformation of the building and foundation movement indicates complete damage [53].

4. Results and discussion

In this section, we first present the displacement results at the ground and building level, and then proceed to derive and discuss the corresponding building damage levels.

Ground-level displacements The pre and post ground point clouds were divided into windows based on their X and Y coordinates. Additionally, we incorporated observation points within a buffer of 10 m around windows of the post-event cloud. This was necessary to ensure that all topography features present in the pre-event cloud remained included in the post-event cloud as the two clouds were not yet aligned. To align the ground point clouds, windows were progressively moved across the analysed area by increments of a given size. These increments are here defined as steps. We initially adopted window and step size values of 100 m and 25 m,

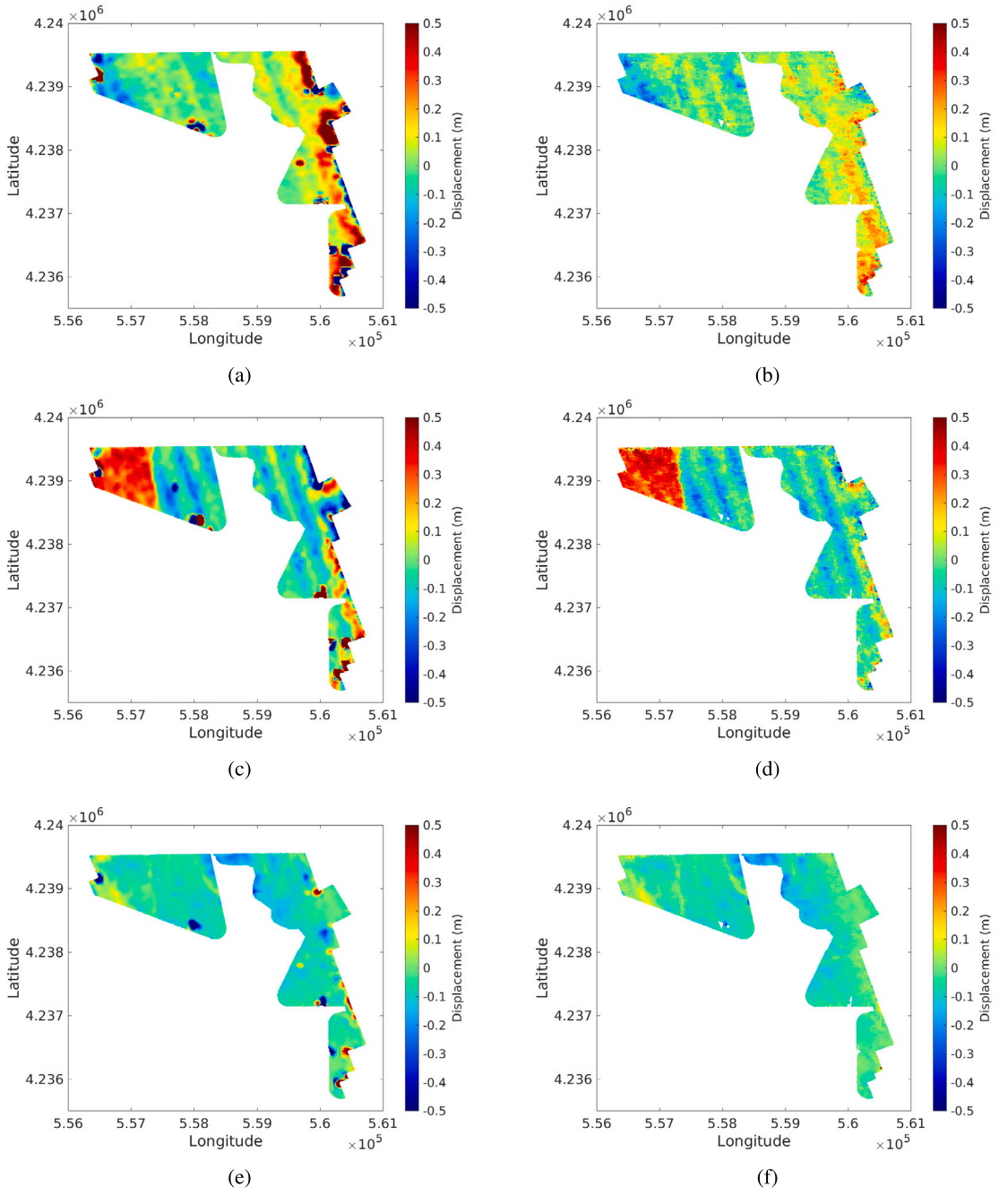

Fig. 4. LiDAR-derived ground displacement maps in (a) X, (c) Y, and (e) Z directions. Figures (b), (d) and (f) show the corresponding maps where false correspondence pairs were removed (Section 3). (For interpretation of the references to colour in this figure legend, the reader is referred to the web version of this article.)

respectively, as proposed by Zhang [28]. This led to a window-side overlap of 75 m between two consecutive windows, ensuring smooth continuity in the displacement pattern. Smaller step sizes led to larger overlaps, further enhancing the smoothness of displacements. This was tested by considering different step sizes of 25, 50, and 75 m, while maintaining a fixed window size of 100 m. Additionally, we tested different window sizes, such as 30, 50, 100, and 200 m, to assess their impact on the final results. Results showed similar patterns and magnitudes of deformation, indicating no significant dependence on the window size. Consequently, we adopted the initial window and step sizes of 100 m and 25 m, respectively, to estimate the ground displacements. Fig. 4 shows the resulting maps of 3D ground displacements induced by the South Napa earthquake.

The ground results show that most of the displacement occurred in the Y direction, with the largest amount of movement found on the left side of the fault. This agrees with the in-situ ground motion observations, indicating that the earthquake primarily exhibited a right-lateral strike-slip behaviour [27]. Similar studies conducted in the Browns Valley area to estimate the ground displacement support these findings. For example, Lyda et al. [29] also obtained a comparable right-lateral pattern and magnitude of displacements. However, their results indicated some areas where the ground surface on both sides of the main rupture showed movements in the same direction. In contrast, our study demonstrated a distinct discontinuity in the displacement pattern, accurately representing the location of the fault rupture. This discrepancy may arise from differences in the weighting procedures for corresponding pairs in the ICP registration. Another study conducted by Ekhtari and Glennie [55] also identified a discernible displacement pattern, despite applying different data preparations and using unweighted least squares to minimise the MSE. Their results showed a smoother and higher resolution of displacements as a smaller window size of 64 m and a step size of 8 m were used during processing.

As shown in Figs. 4(a), 4(c) and 4(e), some areas exhibit significantly larger amounts of displacements, represented by dark blue or dark red colours. These regions correspond to locations where no post-event data were available, resulting in inaccurate point correspondences within the reference data cloud. To address this issue, false corresponding pairs were eliminated during the rejection step described in Section 3. In this step, pairs of points with a distance exceeding 30 cm and normal vectors having an angle larger than the average normal angle of all corresponding pairs within the window were excluded. The resulting ground displacement maps, post-rejection step, are presented in Figs. 4(b), 4(d), and 4(f).

The ground displacements (Fig. 4) reveal a distinct regular pattern of movements in horizontal directions. This pattern is compatible with a systematic error in the X and particularly in the Y component, which appears to be correlated with the flight line direction of the pre-event survey. This suggests the presence of pre-processing errors in the pre-event LiDAR point cloud. Investigating these systematic errors would require access to raw LiDAR data and navigation information from the pre-event survey [56], which were not available for the current study. Although this possible systematic error could introduce bias in both the ground and building displacement measurements, its impact on the final estimations of building drift measurements is expected to be minimal. Since the error affects both ground and building measurements, it is presumed to be neutralised when subtracting the ground displacements from the building displacements to calculate the residual building displacements. Additionally, any remaining random errors were mitigated by averaging the residual building displacements to estimate the drifts.

Building drifts and damage assessment We processed 684 buildings extracted from the OSM [43] and the Napa municipality [44] data layers. After extracting the building points, we separately aligned the pre- and post-event roof points using the point-based ICP approach. The ICP registration estimates the shifts and rotations between the two building clouds, providing building displacement vectors. To illustrate the effectiveness of the ICP alignment, we depicted the distribution of roof points (for one random building in the area) before and after the ICP registration in Fig. 5. This visualisation confirms that the ICP process effectively aligned the pre- and post-event point observations. Furthermore, Fig. 6 shows the location of building roof points for an individual building, along with the distribution of the ground points within a buffer of 4 m around the building. The estimated Y displacement components for the building roof points are visualised using a colour gradient, with the scale ranging from smaller (red) to larger (blue) values.

To estimate the drift ratio for each building, we computed the residual building displacements by subtracting the average ground displacement component from the building measurements. The histograms of these residual building displacements in horizontal directions are presented in Fig. 7. The majority of buildings exhibited small residuals. The large residual displacement displayed for some buildings might be also attributed to the presence of tree leaves on top of the buildings. The classification of trees with heights similar to the building roofs as roof points can lead to a bias in the building displacement vectors. This issue could be addressed by incorporating optical RGB information from the observations to identify tree points accurately and remove them from the building roofs, further enhancing the accuracy of the results. A level of damage was then assigned to each building by estimating the drift ratios and classifying them into five levels of damage, as described in Section 3. These damage categories are specific to light-frame wood constructions designed for specific seismic zones in California. Therefore, they may not be directly applicable to other case studies in different regions or construction types.

The map and distribution of obtained damage levels are illustrated in Figs. 8 and 9, respectively. Fig. 8 visually represents building damage levels by colours ranging from green to red, indicating varying degrees of damage in the Napa Valley area. The map highlights that most of the building damage across the area of interest falls into moderate levels of damage. This observation is further supported by Fig. 9, which shows that the majority of buildings exhibit negligible to moderate damage, with only a few classified as extensively damaged. Specifically, the percentage distribution of obtained damage levels is approximately as follows: negligible damage 27.8%, slight damage 28.3%, moderate damage 38.5%, extensive damage 5.2%, and complete damage 0.1%.

5. Validation

The field datasets were used to validate the ground displacements followed by an evaluation of obtained building damage levels.

Ground displacement validation To quantitatively validate the ground displacement estimation, we compared these results with the field data independently acquired by the USGS team [27]. The USGS observations included measurements of right-lateral offsets at several locations along the fault strands. During the field survey, the largest lateral offsets were observed along the longest fault strand on the west of the Napa Valley (trace A in Fig. 10(a)). The maximum displacement of 46 cm was recorded approximately 10 km from the epicentre towards the northwest [27]. Additionally, the slip observations on trace A included both co-seismic and afterslip measurements.

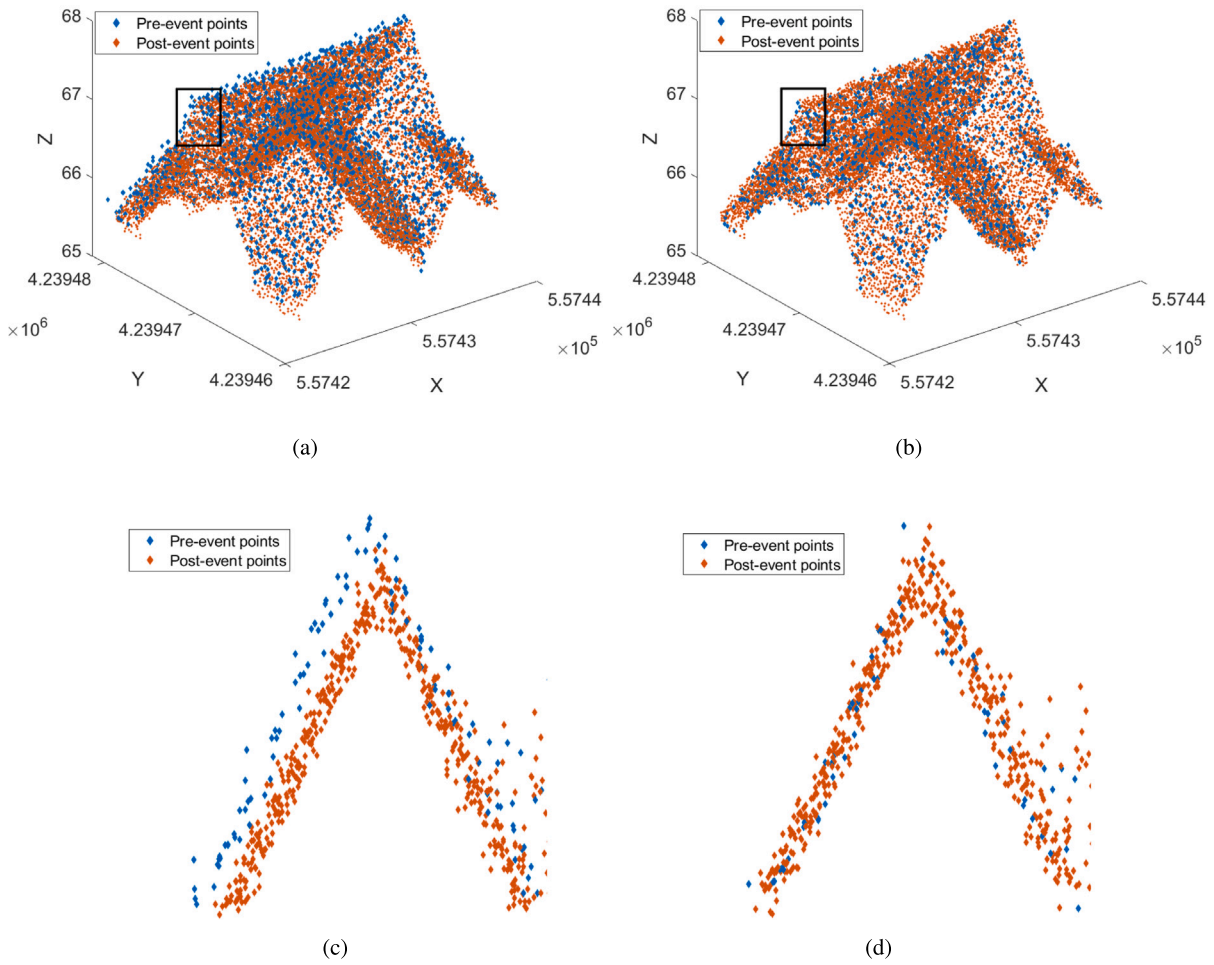

Fig. 5. An example of the distribution of building roof points for (a) before and (b) after the ICP registration. Figures (c) and (d) are close-up views of before and after the ICP registration for one of the roof corners which is shown by black rectangles in Figures (a) and (b).

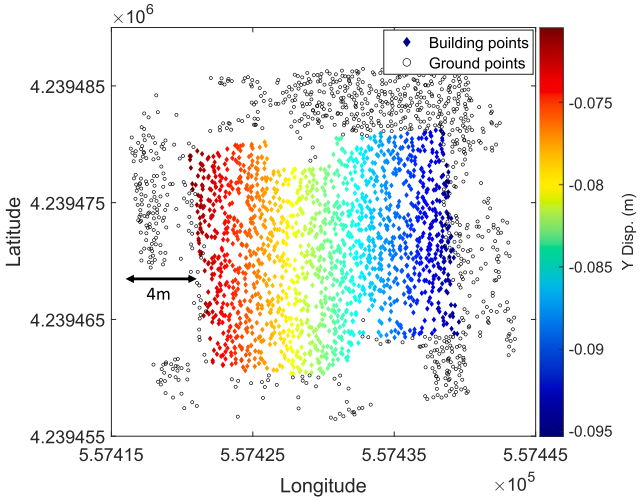

Fig. 6. An example of a 2D map of building roof Y displacements. Displacements of the ground points within a buffer of 4 m around the buildings were used to estimate the residual building displacements. (For interpretation of the references to colour in this figure legend, the reader is referred to the web version of this article.)

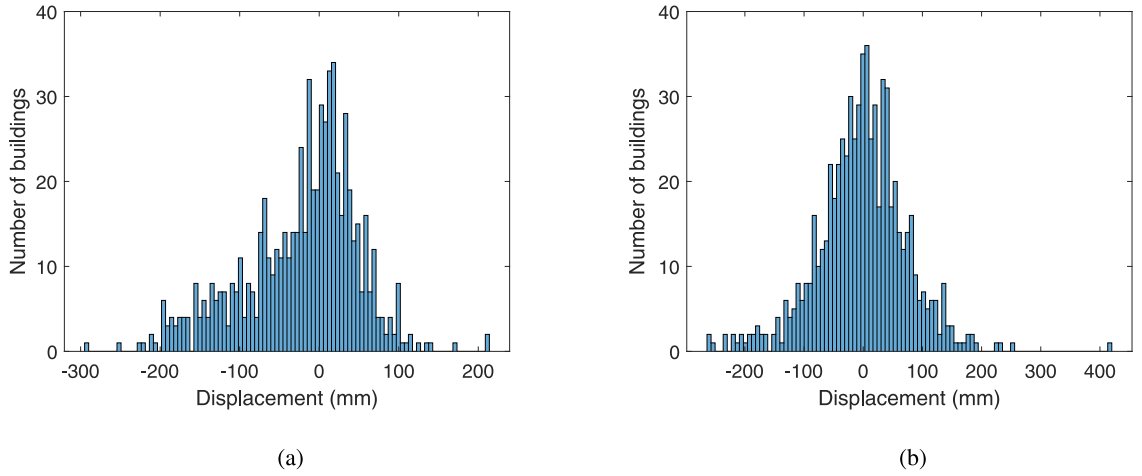

Fig. 7. Distribution of residual building displacements in (a) X and (b) Y directions for all buildings in our area of interest. The residual building displacements were obtained by subtracting the average ground displacements within a buffer of 4 m around each building.

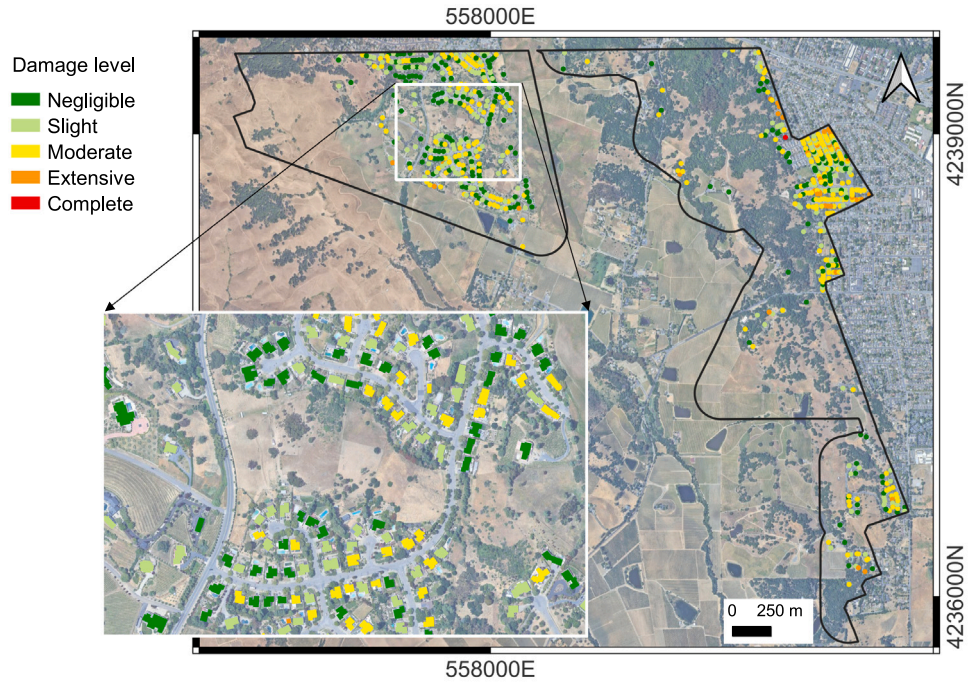

Fig. 8. Building damage map. Building damage levels are based on the residual drift ratios derived from LiDAR displacement measurements. (For interpretation of the references to colour in this figure legend, the reader is referred to the web version of this article.)

Fig. 10(a) shows the locations inspected in the field along trace A, as documented by Hudnut et al. [27]. The offset observation of 36 cm was within the area of interest. For a comprehensive evaluation, we analysed a range of displacement magnitudes along the fault strand within the area of interest. To achieve this, perpendicular cross-sections, each with a length of 200 m, were created at intervals of 50 m, resulting in 20 cross lines (Fig. 10(b)).

For the cross-section displacement estimation, we defined a 1-m-wide buffer on either side of each cross-section and extracted the displacement points within the corresponding buffer regions. We included in the cross-section displacement estimation points within 100 m on each side of the rupture, as significant relative displacements attributable to the fault rupture were not observed further away from the fault. The average magnitudes of Y-direction displacement were then calculated along each side of each

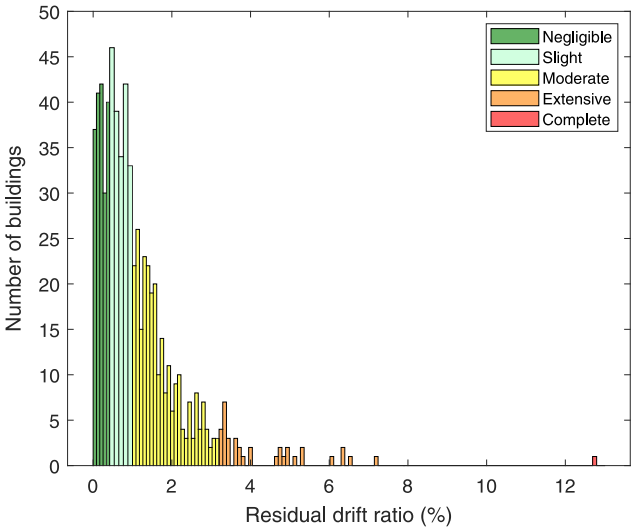

Fig. 9. Distribution of building damage levels in the region of interest. (For interpretation of the references to colour in this figure legend, the reader is referred to the web version of this article.)

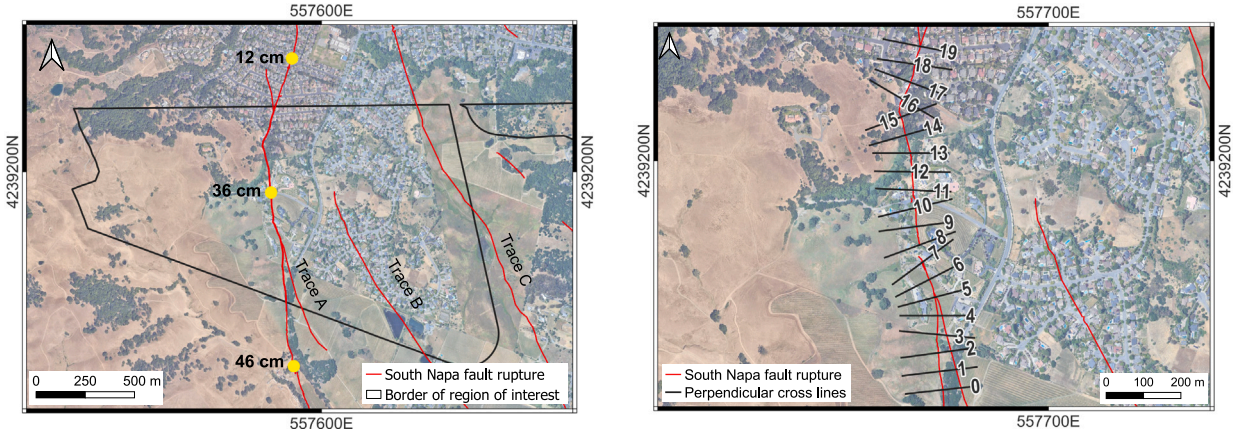

Fig. 10. (a) In-situ right-lateral displacements along trace A, showing the maximum measured slip in the selected sites, rounded to the nearest cm [27] (more detailed surface rupture measurements along fault ruptures are also available in Ponti et al. [42]) and (b) cross-sections along trace A.

cross-section. To obtain the offset of Y-direction displacements for each cross-section, we subtracted the average magnitude on the right side from the average magnitude on the left side. As the LiDAR-derived measurements were in the geographical coordinate system, the offsets were estimated along the north–south direction.

To compare these estimated offsets with the ground measurements, we projected them to the fault direction using the angle between the offset displacement vector and the fault line. For example, Fig. 11 shows the spatial profile of displacement measurements along cross-section number 10 within the 200 m length. The displacement profile shows an offset of about 37 cm along the north–south direction, which corresponds to 35 cm when projected along the fault rupture direction.

Table 1 shows all the offset measurements parallel to the fault rupture. The range of magnitudes along the fault, from south to north (number 0 to 19) is in good agreement with the field observations. More specifically, offset numbers 10 and 11 correspond to the area of the in-situ measurement of 36 cm. The average magnitude of these offsets obtained by LiDAR data is 35.1 cm. This consistency indicates that the LiDAR-derived ground displacement is reliable for further analysis, specifically for quantifying the damage level for each building using residual building displacements.

We employed an additional coding source to evaluate the obtained results. Specifically, we used the Point Data Abstraction Library (PDAL), an open-source Python library designed for LiDAR data processing, as described in [57]. In their research, the authors used PDAL's Python extension to quantify ground deformation following the 2014 Napa earthquake. They analysed pre-

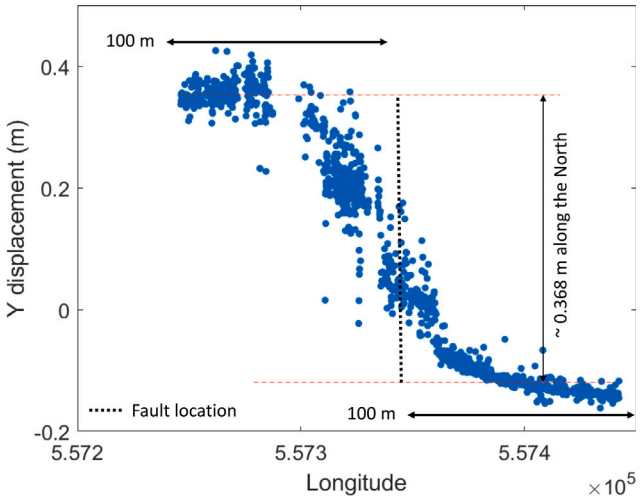

Fig. 11. Spatial profile of ground displacements along the cross-section number 10 shown in Fig. 10(b). The black dashed line indicates the fault rupture location.

Table 1
Offset measurements parallel to the fault rupture along the cross-sections represented in Fig. 10(b).

Cross-section number	LiDAR-derived offsets parallel to the fault (cm)
0	23.20
1	25.20
2	27.01
3	31.30
4	31.00
5	29.07
6	30.05
7	27.05
8	29.30
9	37.50
10	35.40
11	34.90
12	40.60
13	37.80
14	39.70
15	28.40
16	19.60
17	18.50
18	23.70
19	17.30

and post-event airborne LiDAR point cloud data using an ICP algorithm. To ensure consistency, we focused on the same region of interest within the extent of our data coverage and replicated the parameters outlined in [57]. Our analysis produced outcomes that demonstrated similar patterns and magnitudes of displacements as observed in [57].

Building damage validation To validate the building-level results, we used information from tagged buildings as outlined in Section 2. As shown in Fig. 12, the distribution of LiDAR-derived damage levels for the yellow-tagged buildings mostly fell in the range of negligible, slight, and moderate levels. This is in agreement with the field damage observations. LiDAR-based results indicated complete damage only for one of the buildings, which does not correspond to the field-based red-tagged. The field-based red-tagged building was classified as a moderately damaged building based on LiDAR observations. As the building classified as completely damaged from LiDAR observation was not tagged, and no further information was available on the red-tagged building, no speculation can be made on the reasons for discrepancies in these two individual cases.

While the validation confirmed the effectiveness of the method in detecting moderate damage levels and its applicability to the analysed building typology, it is advisable to extend future applications to a broader array of field observations and various building typologies to generalise these findings. Given its emphasis on assessing moderate damage through building drift evaluation, this approach is complementary to damage detection and classification methods that utilise SAR, optical satellite, or LiDAR elevation data, which are primarily concerned with identifying severely damaged and collapsed structures.

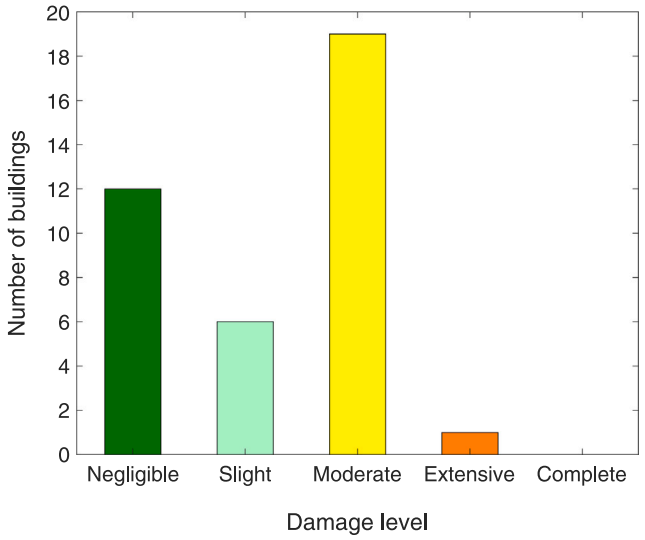

Fig. 12. Distribution of the 38 yellow-tagged buildings in the region of interest. (For interpretation of the references to colour in this figure legend, the reader is referred to the web version of this article.)

A current limitation of the method is the necessity for both pre- and post-event LiDAR data. When pre-event LiDAR data is not available, alternative sources of pre-event data can be used, including aerial imagery, or high-resolution DSMs. It is possible to generate 3D point clouds through photogrammetry methods [58] using these alternative sources of data, although their accuracy depends on factors such as the resolution of the imagery, the quality of the DSM, and the processing techniques employed.

Furthermore, the rising number of government initiatives worldwide committed to the active collection of LiDAR data for diverse purposes, ranging from topographic mapping and land use planning to environmental monitoring and disaster management [59–63], suggests expanding opportunities for the wider application of this method in evaluating structural damage in the future.

6. Conclusion

This research presents a new methodology for the regional scale quantitative assessment of earthquake-induced building damage using remote sensing LiDAR point cloud data. The proposed method allows for the detection of moderate levels of damage, which is typically challenging to identify using other remote sensing techniques. For the first time, the quantification of damage assessment is obtained by integrating LiDAR-derived displacement measurements and a structural engineering parameter, the drift ratio. Using the ICP registration approach, displacement measurements at the building and ground levels are used to estimate drifts and categorise damage levels into negligible to complete damage classes. The proposed methodology is applied to LiDAR data from the 2014 South Napa earthquake in California, demonstrating its effectiveness in detecting moderate levels of damage at a regional scale. The study highlights the potential of using LiDAR-based displacement measurements in conjunction with structural analysis approaches for faster and more accurate post-earthquake damage assessment over large areas.

CRediT authorship contribution statement

Fatemeh Foroughnia: Conceptualization, Data curation, Formal analysis, Investigation, Methodology, Validation, Visualization, Writing – original draft, Writing – review & editing. **Valentina Macchiarulo:** Conceptualization, Methodology, Validation, Visualization, Writing – review & editing. **Luis Berg:** Data curation, Writing – review & editing. **Matthew DeJong:** Conceptualization, Methodology, Writing – review & editing. **Pietro Milillo:** Conceptualization, Data curation, Writing – review & editing. **Kenneth W. Hudnut:** Conceptualization, Data curation, Writing – review & editing. **Kenneth Gavin:** Supervision, Writing – review & editing. **Giorgia Giardina:** Conceptualization, Methodology, Resources, Supervision, Writing – review & editing.

Declaration of competing interest

The authors declare that they have no known competing financial interests or personal relationships that could have appeared to influence the work reported in this paper.

Data availability

The authors do not have permission to share data.

References

[1] D. Guha-Sapir, R. Below, P. Hoyois, EM-DAT: the emergency events database-université catholique de Louvain (UCL)-CRED, 2018, Retrieved from emdat.be.
[2] R. Spence, A. Coburn, Earthquake Protection, second ed., Wiley-Blackwell, Hoboken, NJ, 2002.
[3] J. Macabuag, C. Altheim, S. Thorvaldsdottir, D. Perks, Damage assessments by international engineers following the Albania earthquake of november 2019, Int. J. Disaster Risk Reduct. 72 (2022) 102822.
[4] S. Ghaffarian, S. Emtehani, Monitoring urban deprived areas with remote sensing and machine learning in case of disaster recovery, Climate 9 (4) (2021) 58.
[5] M.R. Whitworth, G. Giardina, C. Penney, L. Di Sarno, K. Adams, T. Kijewski-Correa, J. Black, F. Foroughnia, V. Macchiarulo, P. Milillo, et al., Lessons for remote post-earthquake reconnaissance from the 14 august 2021 Haiti earthquake, Front. Built Environ. (2022) 53.
[6] J.F. Falorca, J.P. Miraldes, J.C.G. Lanzinha, New trends in visual inspection of buildings and structures: Study for the use of drones, Open Eng. 11 (1) (2021) 734–743.
[7] S. Voigt, T. Kemper, T. Riedlinger, R. Kiefl, K. Scholte, H. Mehl, Satellite image analysis for disaster and crisis-management support, IEEE Trans. Geosci. Remote Sens. 45 (6) (2007) 1520–1528.
[8] Y. Du, L. Gong, Q. Li, F. Wu, Earthquake-induced building damage assessment on SAR multi-texture feature fusion, in: IGARSS 2020-2020 IEEE International Geoscience and Remote Sensing Symposium, IEEE, 2020, pp. 6608–6610.
[9] F. Eslamizade, H. Rastiveis, N.K. Zahraee, A. Jouybari, A. Shams, Decision-level fusion of satellite imagery and LiDAR data for post-earthquake damage map generation in Haiti, Arab. J. Geosci. 14 (2021) 1–16.
[10] L. Ge, A.H.-M. Ng, X. Li, Y. Liu, Z. Du, Q. Liu, Near real-time satellite mapping of the 2015 Gorkha earthquake, Nepal, Ann. GIS 21 (3) (2015) 175–190.
[11] L. Gong, C. Wang, F. Wu, J. Zhang, H. Zhang, Q. Li, Earthquake-induced building damage detection with post-event sub-meter VHR TerraSAR-X staring spotlight imagery, Remote Sens. 8 (11) (2016) 887.
[12] M. Ji, L. Liu, M. Buchroithner, Identifying collapsed buildings using post-earthquake satellite imagery and convolutional neural networks: A case study of the 2010 Haiti earthquake, Remote Sens. 10 (11) (2018) 1689.
[13] Y. Bai, B. Adriano, E. Mas, S. Koshimura, Machine learning based building damage mapping from the ALOS-2/PALSAR-2 SAR imagery: Case study of 2016 Kumamoto earthquake, J. Disaster Res. 12 (sp) (2017) 646–655.
[14] O.L. Stephenson, T. Köhne, E. Zhan, B.E. Cahill, S.-H. Yun, Z.E. Ross, M. Simons, Deep learning-based damage mapping with InSAR coherence time series, IEEE Trans. Geosci. Remote Sens. 60 (2021) 1–17.
[15] S. Karimzadeh, M. Matsuoka, M. Miyajima, B. Adriano, A. Fallahi, J. Karashi, Sequential SAR coherence method for the monitoring of buildings in Sarpole-Zahab, Iran, Remote Sens. 10 (8) (2018) 1255.
[16] N. Tamkuan, M. Nagai, Fusion of multi-temporal interferometric coherence and optical image data for the 2016 Kumamoto earthquake damage assessment, ISPRS Int. J. Geo-Inf. 6 (7) (2017) 188.
[17] R. Anniballe, F. Noto, T. Scalia, C. Bignami, S. Stramondo, M. Chini, N. Pierdicca, Earthquake damage mapping: An overall assessment of ground surveys and VHR image change detection after L'Aquila 2009 earthquake, Remote Sens. Environ. 210 (2018) 166–178.
[18] L. Moya, F. Yamazaki, W. Liu, M. Yamada, Detection of collapsed buildings from lidar data due to the 2016 Kumamoto earthquake in Japan, Nat. Hazards Earth Syst. Sci. 18 (1) (2018) 65–78.
[19] W. Liu, F. Yamazaki, Extraction of collapsed buildings due to the 2016 Kumamoto, Japan, earthquake using two-temporal lidar data, in: Lidar Remote Sensing for Environmental Monitoring XVI, Vol. 10779, SPIE, 2018, pp. 153–159.
[20] L. Saganeiti, F. Amato, G. Nolè, M. Vona, B. Murgante, Early estimation of ground displacements and building damage after seismic events using SAR and LiDAR data: The case of the Amatrice earthquake in central Italy, on 24th august 2016, Int. J. Disaster Risk Reduct. 51 (2020) 101924.
[21] E. Nissen, A.K. Krishnan, J.R. Arrowsmith, S. Saripalli, Three-dimensional surface displacements and rotations from differencing pre-and post-earthquake LiDAR point clouds, Geophys. Res. Lett. 39 (16) (2012).
[22] S. Ghaffarian, N. Kerle, T. Filatova, Remote sensing-based proxies for urban disaster risk management and resilience: A review, Remote Sens. 10 (11) (2018) 1760.
[23] E. Miranda, C.J. Reyes, Approximate lateral drift demands in multistory buildings with nonuniform stiffness, J. Struct. Eng. 128 (7) (2002) 840–849.
[24] K. Dai, J. Wang, B. Li, H. Hong, Use of residual drift for post-earthquake damage assessment of RC buildings, Eng. Struct. 147 (2017) 242–255.
[25] M. Gaetani d'Aragona, M. Polese, E. Cosenza, A. Prota, Simplified assessment of maximum interstory drift for RC buildings with irregular infills distribution along the height, Bull. Earthq. Eng. 17 (2) (2019) 707–736.
[26] A. Ghobarah, On drift limits associated with different damage levels, in: International Workshop on Performance-Based Seismic Design, Vol. 28, Department of Civil Engineering, McMaster University Ontario, Canada, 2004.
[27] K.W. Hudnut, T.M. Brocher, C.S. Prentice, J. Boatwright, B.A. Brooks, B.T. Aagaard, J.L. Blair, J. Fletcher, J.E. Erdem, C.W. Wicks, et al., Key Recovery Factors for the August 24, 2014, South Napa Earthquake, Vol. 10, US Department of the Interior, US Geological Survey, 2014.
[28] X. Zhang, Lidar-Based Change Detection for Earthquake Surface Ruptures (Ph.D. thesis), University of Houston, 2016.
[29] A. Lyda, X. Zhang, C. Glennie, K. Hudnut, B. Brooks, Airborne light detection and ranging (LIDAR) derived deformation from the MW 6.0 24 august, 2014 South Napa earthquake estimated by two and three dimensional point cloud change detection techniques, Int. Arch. Photogramm. Remote Sens. Spatial Inf. Sci. 41 (2016).
[30] C.P. Scott, J.R. Arrowsmith, E. Nissen, L. Lajoie, T. Maruyama, T. Chiba, The M7 2016 Kumamoto, Japan, earthquake: 3-D deformation along the fault and within the damage zone constrained from differential lidar topography, J. Geophys. Res.: Solid Earth 123 (7) (2018) 6138–6155.
[31] M. Raffel, C.E. Willert, J. Kompenhans, et al., Particle Image Velocimetry: A Practical Guide, vol. 2, Springer, 1998.
[32] S. Mukoyama, Estimation of ground deformation caused by the earthquake (M7. 2) in Japan, 2008, from the geomorphic image analysis of high resolution LiDAR DEMs, J. Mt. Sci. 8 (2) (2011) 239–245.
[33] A. Borsa, J.-B. Minster, Rapid determination of near-fault earthquake deformation using differential LiDAR, Bull. Seismol. Soc. Am. 102 (4) (2012) 1335–1347.
[34] L. Moya, F. Yamazaki, W. Liu, T. Chiba, Calculation of coseismic displacement from lidar data in the 2016 Kumamoto, Japan, earthquake, Nat. Hazards Earth Syst. Sci. 17 (1) (2017) 143–156.
[35] D. Ishimura, S. Toda, S. Mukoyama, S. Homma, K. Yamaguchi, N. Takahashi, 3D surface displacement and surface ruptures associated with the 2014 Mw 6.2 Nagano earthquake using differential Lidar3D surface displacement and surface ruptures, Bull. Seismol. Soc. Am. 109 (2) (2019) 780–796.
[36] P.J. Besl, N.D. McKay, Method for registration of 3-D shapes, in: Sensor Fusion IV: Control Paradigms and Data Structures, Vol. 1611, SPIE, 1992, pp. 586–606.
[37] Y. Chen, G. Medioni, Object modelling by registration of multiple range images, Image Vis. Comput. 10 (3) (1992) 145–155.
[38] T. Zieher, M. Bremer, M. Rutzinger, J. Pfeiffer, P. Fritzmann, V. Wichmann, Assessment of landslide-induced displacement and deformation of above-ground objects using UAV-borne and airborne laser scanning data, ISPRS Ann. Photogramm. Remote Sens. Spatial Inf. Sci. 4 (2019).
[39] Cal OES, August 24, 2014 south napa earthquake, 2014, URL: https://www.caloes.ca.gov/.
[40] USGS, M 6.0 South Napa, 2014, URL: https://earthquake.usgs.gov/earthquakes/eventpage/nc72282711/executive#summary.

[41] T.M. Brocher, A.S. Baltay, J.L. Hardebeck, F.F. Pollitz, J.R. Murray, A.L. Llenos, D.P. Schwartz, J.L. Blair, D.J. Ponti, J.J. Lienkaemper, et al., The M w 6.0 24 august 2014 south napa earthquake, Seismol. Res. Lett. 86 (2A) (2015) 309–326.
[42] D.J. Ponti, C.M. Rosa, J.L. Blair, The Mw 6.0 South Napa Earthquake of August 24, 2014—Observations of Surface Faulting and Ground Deformation, with Recommendations for Improving Post-Earthquake Field Investigations, Technical Report, US Geological Survey, 2019.
[43] OpenStreetMap, 2020, URL: https://www.openstreetmap.org.
[44] County of Napa, GIS data catalog, 2021, URL: http://gis.napa.ca.gov/giscatalog/.
[45] EERI, M 6.0 South Napa, Calfornia Earthquake of August 24, 2014, Technical Report, in: EERI Special Earthquake Report, California Earthquake Clearinghouse, 2014.
[46] J. Boatwright, J.L. Blair, B.T. Aagaard, K. Wallis, The distribution of red and yellow tags in the city of Napa, Seismol. Res. Lett. 86 (2A) (2015) 361–368.
[47] P. Heresi, E. Miranda, Fragility curves and methodology for estimating postearthquake occupancy of wood-frame single-family houses on a regional scale, J. Struct. Eng. 147 (5) (2021) 04021039.
[48] OpenTopography, August 24, 2014 south Napa earthquake, 2014, URL: https://doi.org/10.5069/G9F769H3.
[49] S. DeLong, 2014 South Napa Earthquake Airborne Lidar Reprocessing Notes, USGS Earthquake Science Center, 2014.
[50] LAStools, Efficient LiDAR processing software (version 1.4), 2019, URL: http://rapidlasso.com/LAStools.
[51] J.H. Friedman, F. Baskett, L.J. Shustek, An algorithm for finding nearest neighbors, IEEE Trans. Comput. 100 (10) (1975) 1000–1006.
[52] A. Diederichs, E. Nissen, L. Lajoie, R. Langridge, S. Malireddi, K. Clark, I. Hamling, A. Tagliasacchi, Unusual kinematics of the papatea fault (2016 Kaikōura earthquake) suggest anelastic rupture, Sci. Adv. 5 (10) (2019) eaax5703.
[53] B.R. Ellingwood, D.V. Rosowsky, W. Pang, Performance of light-frame wood residential construction subjected to earthquakes in regions of moderate seismicity, J. Struct. Eng. 134 (8) (2008) 1353–1363.
[54] FEMA, Multi-Hazard Loss Estimation Methodology, Earthquake Model, Technical Report, Federal Emergency Management Agency, Washington, D.C., 2006.
[55] N. Ekhtari, C. Glennie, High-resolution mapping of near-field deformation with airborne earth observation data, a comparison study, IEEE Trans. Geosci. Remote Sens. 56 (3) (2017) 1598–1614.
[56] C.L. Glennie, A. Hinojosa-Corona, E. Nissen, A. Kusari, M.E. Oskin, J.R. Arrowsmith, A. Borsa, Optimization of legacy lidar data sets for measuring near-field earthquake displacements, Geophys. Res. Lett. 41 (10) (2014) 3494–3501.
[57] H. Butler, B. Chambers, P. Hartzell, C. Glennie, PDAL: An open source library for the processing and analysis of point clouds, Comput. Geosci. 148 (2021) 104680.
[58] N. Cenni, S. Fiaschi, M. Fabris, Integrated use of archival aerial photogrammetry, GNSS, and InSAR data for the monitoring of the patigno landslide (northern apennines, Italy), Landslides 18 (2021) 2247–2263.
[59] OpenTopography, Find topography data, 2024, URL: https://portal.opentopography.org/datasets.
[60] USGS, USGS, 2024, URL: https://www.usgs.gov/faqs/what-lidar-data-and-where-can-i-download-it.
[61] NEON, National ecological observatory network, explore data products, 2024, URL: https://data.neonscience.org/data-products/explore.
[62] Natural Resources Canada, Natural resources Canada, 2024, URL: https://natural-resources.canada.ca/home.
[63] European Data, European data, 2024, URL: https://data.europa.eu/en.